ADVANCED FUNCTIONAL MATERIALS
www.afm-journal.de

www.MaterialsViews.com

Water-Induced Phase Separation Forming Macrostructured Epitaxial Quartz Films on Silicon

Glenna L. Drisko, Adrian Carretero-Genevrier, Martí Gich, Jaume Gàzquez, Djawhar Ferrah, David Grosso, Cédric Boissière, Juan Rodriguez-Carvajal, and Clément Sanchez**

Quartz has been widely used as a bulk material in optics, the microelectronic industry, and sensors. The nanostructuring and direct integration of oriented quartz crystals onto a semiconductor platform has proven to be challenging. However, here, a new approach is presented to integrate epitaxial quartz films with macroperforations within the range of 500 nm and 1 μm using chemical solution deposition. This method constitutes an appealing approach to develop piezoelectric mass sensors with enhanced resonance frequencies due to the thickness reduction. Perforated quartz films on (100)-silicon are prepared from amorphous silica films deposited via dip-coating and doped with metal cations that catalyze quartz crystallization. The metal cations are also active in the formation of the macroperforations, which arise due to a phase separation mechanism. Cationic surfactant–anion–metal cation assemblies stabilize droplets of water, creating an indentation in the hydrophilic silica matrix which remains after solvent evaporation. Many cations induce phase separation, including Li^+, Na^+, Sr^{2+}, Mn^{2+}, Fe^{2+}/Fe^{3+}, Ca^{2+}, Ce^{3+} and La^{3+} but only the Sr^{2+} and Ca^{2+} cations in this series induce the epitaxial growth of α-quartz films under the conditions studied. The combination of sol–gel chemistry and epitaxial growth opens new opportunities for the integration of patterned quartz on silicon.

1. Introduction

Quartz has many advantages over its amorphous counterpart, including UV transparency, lower solubility in aqueous solutions, increased hardness and piezoelectricity. Thus crystalline silica is used in optics, biomedicine, abrasion and electronics. The high quality factor of quartz for piezoelectricity lends itself to highly sensitive measurements of mass changes monitored via resonance frequency shifts, which enables the quartz crystal microbalance to detect molecular deposition and the study of biological systems by micro-electro-mechanical systems. In the latter case, the micromorphology of the film is of high importance as macroperforations of the correct size distribution can enhance cell attachment and spread.[1]

Due to the previous absence of methods for epitaxial growth of quartz on silicon,[2] quartz-based sensors are currently produced using bulk micromachining, with a minimum obtainable thickness of 10 μm.[3] Reducing the thickness of quartz crystals used for mass sensing is very appealing to increase resonance frequency and improve measurement sensitivity.[3] Quartz patterning can be achieved through wet etching, but precision and miniaturization are limited using this technique. Dry etching via reactive ion etching is another approach with impressive control over morphology,[4] however this technique is relatively expensive and usually requires multiple steps to deposit an effective mask. The incorporation of functional oxide nanostructures as active materials in electronics critically depends on the ability to integrate crystalline oxides onto silicon substrates. The difficulty of assimilating such materials into a device arises from the differences in their crystal structures and chemical reactivity.[4] Thus material scientists and engineers have long awaited a method where amorphous structured silica could be converted to epitaxial quartz.

Dr. G. L. Drisko, Dr. A. Carretero-Genevrier, Prof. D. Grosso, Dr. C. Boissière, Prof. C. Sanchez
Laboratoire de Chimie de la Matière Condensée de Paris
Université Pierre et Marie Curie-Paris 6, CNRS, 4 place Jussieu
75252, Paris CEDEX 05, France
E-mail: adrien.carretero-genevrier@ec-lyon.fr; clement.sanchez@upmc.fr
Dr. A. Carretero-Genevrier, Dr. D. Ferrah
Institut des Nanotechnologies de Lyon (INL)
CNRS- Ecole Centrale de Lyon
36 avenue Guy de Collongue
69134, Ecully, France
Dr. M. Gich, Dr. J. Gàzquez
Institut de Ciència de Materials de Barcelona ICMAB
Consejo Superior de Investigaciones Científicas CSIC
Campus UAB, 08193, Bellaterra, Catalonia, Spain
Prof. J. Rodriguez-Carvajal
Institut Laue-Langevin
6 rue Jules Horowitz, BP 156, 38042,
Grenoble Cedex 9, France

DOI: 10.1002/adfm.201401066

We recently published the first report of the conversion of amorphous silica thin films to epitaxial polycrystalline α-quartz, while maintaining pore architectures.[5] Here we elaborate the synthesis methods for the macrostructured silica films and explore crystallization over a range of conditions. Macroperforations of adjustable size and surface coverage are generated via a nucleation and growth phase separation, mediated by the salt, surfactant and counterion present in solution. This phase separation technique differs from both breath figures and templating salt crystals[6] or organic moieties.[7,8] The interplay between the kinetics of the sol-gel transition and rate of water intake into the film determine the size of the macroperforations, allowing for the preparation of epitaxial quartz films with controllable morphology.

2. Results and Discussion

Macropores were produced in silica films via a salt-surfactant mediated nucleation and growth mechanism. The Si substrate is coated by an amorphous silica film with an opalescent appearance which scatters the light from a green laser to produce a diffraction pattern (**Figure 1**a), indicating the presence of some degree of order and a periodicity comparable with the light wavelength (λ = 532 nm). The films have hierarchical pore structure, as CTA$^+$ organizes into micelles that generate mesopores (3.2 nm, Figure S1), and additionally to assist the phase separation process, which forms macropores. Many salts generated macroperforated films, including monovalent (LiBr and NaBr), divalent ($Sr(NO_3)_2$, $SrCl_2$, $Ca(NO_3)_2$, $MnCl_2$, $FeCl_2$) and trivalent ($CeCl_3$, and $La(NO_3)_2$) cations (Figure S2). Organic salts, such as $N(CH_3)_4Br$, and any salt insoluble in the ethanolic solvent were unsuitable candidates, as ethanol was the primary solvent. Nonionic surfactants (Brij 56, Pluronic F127 and polyethylene-block-polybutadiene) did not produce such macropore structures, thus CTAB was used as the surfactant. Therefore the dissociation of the salt in solution and the ionic nature of the surfactant are key elements of the phase separation mechanism. We present the relevant results that ilucidate the macropore formation mechanism in the following sections: 1. Ultimate cation location, 2. The role of processing parameters, and 3. The role of solution chemistry.

2.1. Ultimate Cation Location

FEG-SEM analysis of films calcined at 500 °C (Figure 1c–h) showed that the salt was predominantly lining the macroperforations (Figure 1c, e, g, h, Figure S3–5). Three cations were imaged, monovalent Na$^+$, divalent Ca^{2+} and trivalent Ce^{3+}, which were chosen based on their excitation energies being significantly different than those of Si and O, and on having excitation energies less than 5 keV. Excitation at 5 keV was the maximum intensity possible as this led the SEM electron beam to penetrate a maximum of 287 nm and the film itself was 245 nm thick. Imaging a cross-section of a film prepared with Sr^{2+} with high resolution STEM, it is possible to see that a fraction of metal salt was additionally present in the silica walls, perhaps due to association with CTAB (Figure S6g).

2.2. The Role of Processing Parameters: Drying Conditions and Film Thickness

Experiments studying the influence of different film preparation parameters were conducted to understand the phase separation mechanism and determine how macropore size, % coverage and density could be controlled (**Figure 2**, Figure S7). First, parameters that affect evaporation were explored, such as ethanol content (data not shown), temperature, and relative humidity. As ethanol content increases, so does the rate of evaporation, but the film thickness also changes, confusing the conclusions. In this series, perforation size decreased with increasing ethanol content, which either means that perforation size increases with film thickness (discussed again below) or that it increases with decreased evaporation rate. Humidity does impact pore size (see next paragraph), but as humidity affects the evaporation rate, the silica condensation kinetics and the quantity of water in the film, this is also an ambiguous result. Regarding the influence of evaporation temperature, there was no significant change in % coverage (Figure 2a), but a 40% decrease in pore diameter was observed between 24 °C and 36 °C due to an increase in the nucleation rate of the perforations (plotted in Figure S7). As the humidity and ethanol results contradict each other in terms of evaporation rate, and as temperature affects nucleation rate more than perforation size, the formation of macropores is not principally an evaporation induced process.

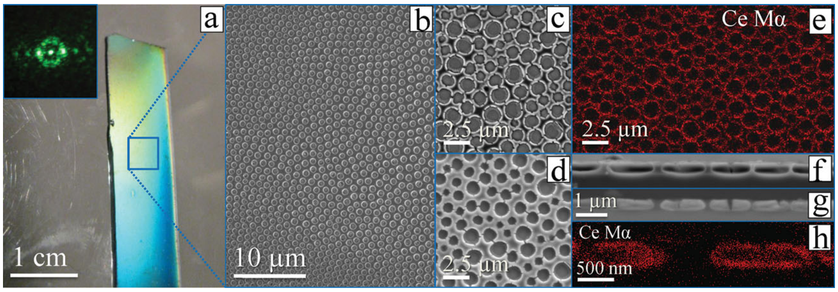

Figure 1. (a) Optical image of a dip-coated macroporous film prepared using 1 mmol $Sr(NO_3)_2$, 25 °C, 40% RH, 2 mm s^{-1}, with a CTAB/Si ratio of 0.14. Inset showing the diffraction pattern of grazing incident light from a green laser λ = 532 nm. (b) SEM low-magnification image of the same film. Film produced using 2.6 mmol $CeCl_3$, 25 °C, 40% RH, 3 mm s^{-1} imaged using (c, g) FEG-SEM back scatter detector, (d, f) secondary electron detector, (e, h) elemental analysis of Ce (Mα = 0.88 keV), where (c-e) are images taken from the top view of the sample, and (f-h) are cross-sectional viewings of the film.

Relative humidity (RH) has a strong effect on pore structures. Under dry conditions, the phase separation did not occur. Humidity is thus needed to generate the macropore structure, and its increase favors larger perforations (Figure 2b). Above 55% RH, the film absorbs so much water that it does not dry and droplets visible to the naked eye form on the substrate, destroying its homogeneity.

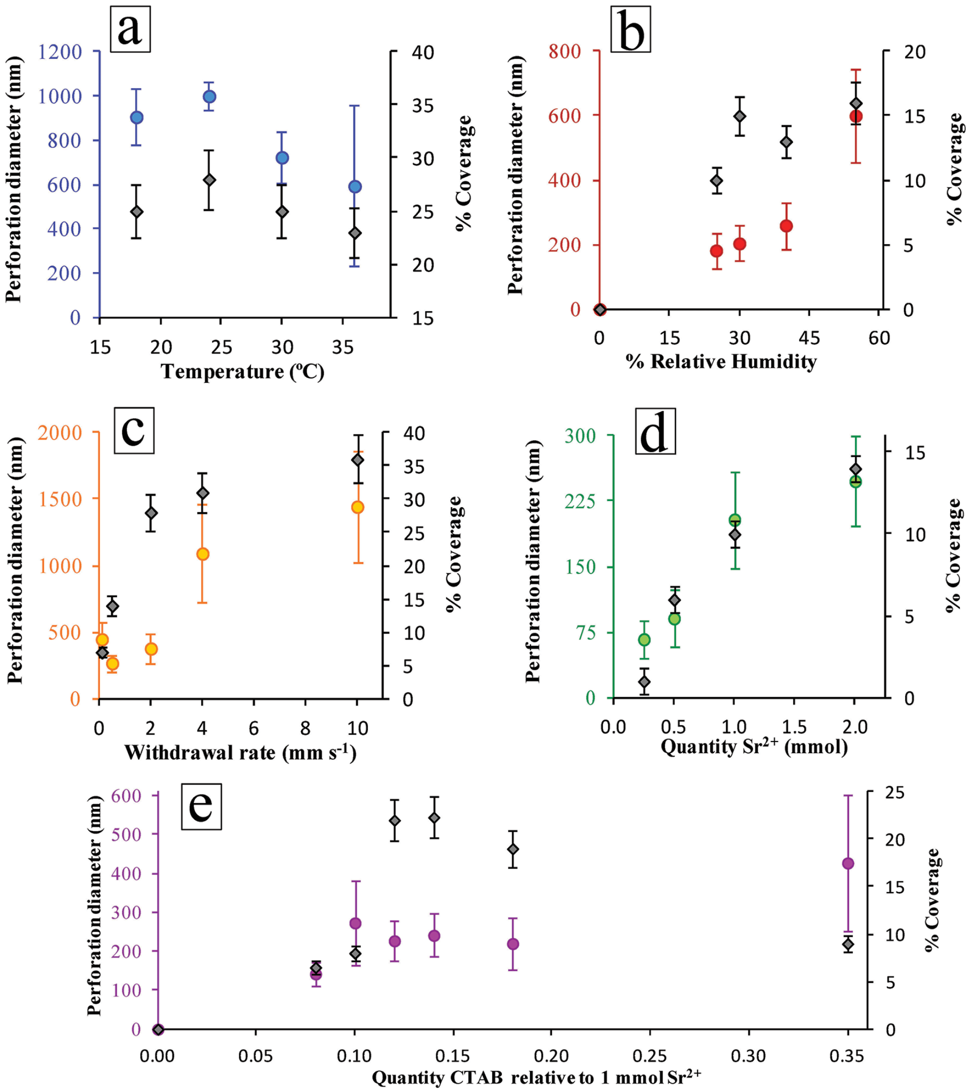

Figure 2. Size of macropores in films. (a) Change in temperature (1 mmol Sr^{2+}, 4 mm s^{-1} withdrawal rate, 40% RH). (b) Change in relative humidity (1 mmol Sr^{2+}, 24 °C, 1 mm s^{-1} withdrawal rate). (c) Change in withdrawal rate (1 mmol Sr^{2+}, 25 °C, 40% RH). (d) Change in strontium quantity (24 °C, 1 mm s-1 withdrawal rate, 30% RH). (e) Change in CTAB concentration (25 °C, 1 mm s^{-1} withdrawal rate, 40% RH). Colored circles relate to the axis bearing perforation diameter, the grey diamonds relate to the % coverage.

It is tempting to attribute these macroperforations to a breath figure, but there are key differences. Firstly, the morphology of the macropores is different than that formed by breath figures. Breath figures produce indentations of between 300 nm-10 µm, larger than those formed in films produced through this phase separation process (75 nm–2 µm). More importantly, the interactions between the water and the film are different. Breath figures are due to indentations formed from the condensation of water droplets on the surface of a hydrophobic film during evaporative cooling in a highly humid environment.[9] In the current report, films are hydrophilic, quickly drawing water from the atmosphere into the poorly condensed silica/CTAB/salt structure of the film (phase separation is taking place typically 1–2 minutes after the film deposition, see video in Supplementary Information). The silica network is still flexible at this time and can accommodate the formation and growth of water droplets. The % coverage of pores globally increases from 0 to 55% RH but evolves little in the 30–55% RH range. In addition, the higher RHs finally produce lower perforations densities per surface area (Figure S7b). Thus, an increasing RH concurrently favors the absorption of water, and diminishes silica condensation kinetics, giving enough time for small droplets to coalesce, minimizing their surface energy, without increasing significantly the % coverage.

Withdrawal rate greatly affects the perforation size (Figure 2c) as film thickness alters with withdrawal speed (Figure S8).[10] Whenever a liquid film is deposited in the Landau-Levich regime (that is dip-coating speeds ≥0.5 mm s^{-1}), thicker films generate larger macropores. Thicker films evaporate more slowly and thus they have more time to absorb a significant amount of water, which mechanically favors the growth of water domains. This is confirmed by the study of pore density (Figure S7c), which decreases for thicker films suggesting once again that with longer drying times droplet coalescence occurs.

Thus all of the processing parameters that affect the crosslinking kinetics of the silica network (drying temperature, RH and film thickness) affect both the droplet domain size, perforation coverage fraction and perforation density per surface area of film.

2.3. The Role of Solution Chemistry: Salt Concentration, Salt Nature, Anions, and Surfactant

Among chemical parameters, salt content is very important. It has a linear affect on both the % coverage and the perforation diameter (Figure 2d). Surprisingly, the amount of salt does not affect the perforation density (Figure S7) for a given processing parameter set. If compared with the influence of processing parameters which affect the condensation kinetics of the silica network (and the number of perforations per surface unit of film), it is very likely that salt does not significantly affect the condensation kinetics of the silica network, but simply controls the kinetics of water absorption. Saltier films produce larger macropores over the same duration of time. To unambiguously prove this point would require specifically designed in situ monitoring of water droplet nucleation and growth. Finally, as Sr^{2+} salts are poorly soluble in ethanol, we could not explore the effect of higher salt concentrations. In fact, aging the solution led to the recrystallization of $Sr(NO_3)_2$ (precipitate verified using XRD). At 25 °C, a solution containing $Sr(NO_3)_2$ had detrimental precipitation within 30 min (followed by DLS measurements and monitoring film quality). Precipitation occurred more quickly for concentrated solutions. The solution temperature also has a large impact on the stability of the solution, with solutions at 30 °C being much more stable than solutions at 18 °C. $SrCl_2$ is more soluble in ethanol than $Sr(NO_3)_2$, providing greater solution longevity (up to 24 h). Solutions of LiBr induced good quality phase separation even after 3 months of aging due to the high solubility of the LiBr in ethanol.

Macroperforated films were prepared using a suite of cations at 25 °C (Figure S2). Very little change was apparent in perforation size, % coverage or morphology. What differences are present can be attributed to the cation solubility and the counterions present in solution. However, dip coating conditions need to be slightly modified for each salt. For example, films containing $Ca(NO_3)_2$ (solubility 121 g/100 g H_2O at 20 °C) did not dry at 22 °C and 40% relative humidity due to the hygroscopicity of the film, whereas these were ideal conditions for films prepared using $Sr(NO_3)_2$ (solubility 66 g/100 g H_2O at 20 °C). Thus conditions must be tuned for each cation, but the structural evolution trends described above are the same for all inorganic salts tested.

A cornerstone to this phase separation mechanism is the counterion. It seems that the anion is perhaps facilitating an interaction between the cationic surfactant and the cationic metal making a $[S^+A^- M^{x+}]$ complex. Several anions are present in solution: Br^- originating from CTAB; the counterion from the acid (HCl, HBr, HNO_3); and the counterion from the salt ($Sr(NO_3)_2$, $SrCl_2$, etc.). Here it is useful to recall the molar ratios of reagents included in a standard solution: 1 Si: 0.14 CTAB: 6.6 H_2O: 25 EtOH: 1 HCl: 0.06 $SrCl_2$ yielding anion atomic ratios of 0.14 A^-_{CTAB} : 1 A^-_{HCl} : 0.12 $A^-_{SrCl_2}$. Thus the largest source of anions comes from the acid by a factor of more than 6. Three different sources of acid were tested, HCl, HBr, HNO_3 (Figure S9). HNO_3 did not produce phase separation, HCl yielded relatively small perforations and HBr led to large perforations. Although it is alluring to ascribe macroperforation size to salt insolubility, to remain consistent with previously reported mechanisms,[11] perforation size does not correlate with solubility in the case of Sr^{2+} salts as the chloride is less soluble than the nitrate salt. The order of solubility in water at 25 °C is $SrCl_2$ (35.4 g 100 mL^{-1}) < $Sr(NO_3)_2$ (44.5 g 100 mL^{-1}) < $SrBr_2$ (51.7 g 100 mL^{-1}).[12] It seems likely that the surface stabilization of the water droplet by an ionic complex formed by ions present in solution can account for the difference in perforation size. Supporting this statement, the destruction of a thin soft matter film lining the perforations in the as-made films is observed using a scanning electron microscope (Figure S10). The degree of surface stabilization by CTAC ($[C_{16}H_{33}N(CH_3)_3{}^+Cl^-]$) is not the same as that of CTAB ($[C_{16}H_{33}N(CH_3)_3{}^+Br^-]$).[13] Electrostatic repulsion between adjacent polar head groups associated with bromide is much lower than those associated with chloride due to the *counterion binding strength*.[13] The observed packing and capacity to assemble of $[CTA^+Br^- M^{x+}]$ is completely different than $[CTA^+Cl^- M^{x+}]$ in that they assemble into different phases and require different conditions in order to assemble. Nitrate is a poor coordinating ligand and cannot simultaneously coordinate a CTA^+ molecule and a Sr^{2+} atom in the $[S^+A^-M^{x+}]$ complex, which therefore prevents the formation of macrodomains. Strontium nitrate salt crystals can be observed in the film produced from HNO_3 (Figure S9c,d). The presence of deposited salt on the walls and floor of the perforation is due to both the formation of the $[S^+A^- M^{x+}]$ complex and the drying of the salty water droplet.

When investigating the role of surfactant, we observed that nonionic block copolymers (Brij, Pluronics, PB-PEO) did not produce phase separation and yielded silica films with the same salt deposits as seen when HNO_3 was used as a source of H^+. The quantity of CTA^+ surfactant also played a role in the perforation size and % coverage (Figure 2e, Figure S1 and S11). At both low and high CTA^+ contents, phase separation was poor, indicating that the optimal ratio of CTA^+/Sr^{2+} lies between 2 and 3. In addition to affecting the phase separation behavior, the surfactant created mesostructuration in the amorphous silica film, as observed using GI-SAXS (Figure S1). CTAB/Si ratios below 0.12 produced wormhole-like structures. From CTAB/Si ratios of 0.12–0.35, 2D hexagonal structures were observed. In the absence of Sr^{2+} salt, the transition from wormhole-like to 2D hexagonal was abrupt and clean, however when salt was present in solution for ratios of 0.12–0.18, a mixture of well-oriented and isotropically oriented mesopores was observed. There are three possible explanations: Sr^{2+} interferes with the CTAB structuration; Sr^{2+} withdraws a portion of CTAB for use in the macroperforations; the CTAB is perfectly ordered, but aligned differently depending on whether it is lining the macropores or the flat portions of the film. This difference in alignment would arise if the CTAB began structuration at the air-liquid interface and then reproduced the structure deeper into the film as the film dried. Initial structuration along the air-liquid interface is observed in aerosols.[14]

Mechanism: The observations reported in the preceding sections indicate that the production of macro-perforations occurs through the nucleation and growth of water droplets within the CTAB/silica hybrid network mediated by the salt and the surfactant (**Figure 3**). To summarize the results:

- The phase separation proceeded for mono-, di- and trivalent cationic salts, where the salts were predominantly deposited on the walls of the perforations, along with a surfactant membrane.
- The surfactant must be itself ionic to produce a phase separation.
- Anions capable of coordinating at least two cations simultaneously were necessary for the phase separation to occur (e.g. Cl^- and Br^-).
- A certain quantity of surfactant, salt and relative humidity are needed. Increases in salt and humidity linearly increase perforation size. Increases in surfactant concentration increase perforation size up to a point, after which more CTAB decreases perforation size.
- Processing parameters that slow SiO_2 condensation kinetics (drying temperature, RH and film thickness) affect perforation size, coverage fraction and perforation density per surface area.

Combining these observations the following mechanism is proposed: In the initial phases of drying CTA^+ micelles organize with Sr^{2+} associated with the polar head groups through an ionic complex of the type $[S^+A^- M^{x+}]$, where S^+ is CTA^+, A^- is the counterion (Br^- or Cl^-) and M^{x+} is the cationic salt (*e.g.* Na^+, Sr^{2+}, Ce^{3+}).[15] M^{x+} and H_2O are distributed through the loosely condensed SiO_2 matrix. Just after deposition, the uncondensed film begins to pump water from the atmosphere. A surfactant bilayer (previously evidenced in the preparation of metallic nanoparticles in aqueous media,[16–18] and silica surfaces in water[19] is likely to ensure the stabilization of the water/silica interface. A $[CTA^+A^-M^{x+}]$ membrane self-assembles at the droplet interface to minimize the interfacial energy. However, when a large excess (greater than 3) of CTAB to cationic salt exists, salt is predominately stabilized by the micelles within the silica walls, and thus water pumping is minimized. The amount of salt present in solution controls the hygroscopicity of the film, thus the kinetics of water absorption. Once a certain amount of water is absorbed, a phase separation occurs via nucleation, mediated by $[S^+A^- M^{x+}]$ species, and growth of water droplets. The growth of water domains is limited by the condensation of the silica network, thus the final macrostructure of the film is not the result of a thermodynamically stable system, but rather from quenching the phase separation of a phase A (water and salt-rich) and a phase B (made of salt and mesostructured silica). Normally on the time frame of the film evolution, spherical droplets are frozen in the silica network. However, if TEOS is added to the solution shortly before film deposition is performed, TEOS is not hydrolyzed and condensation is delayed. In this case spinodal decomposition occurs to form non-spherical structures (Figure S12).

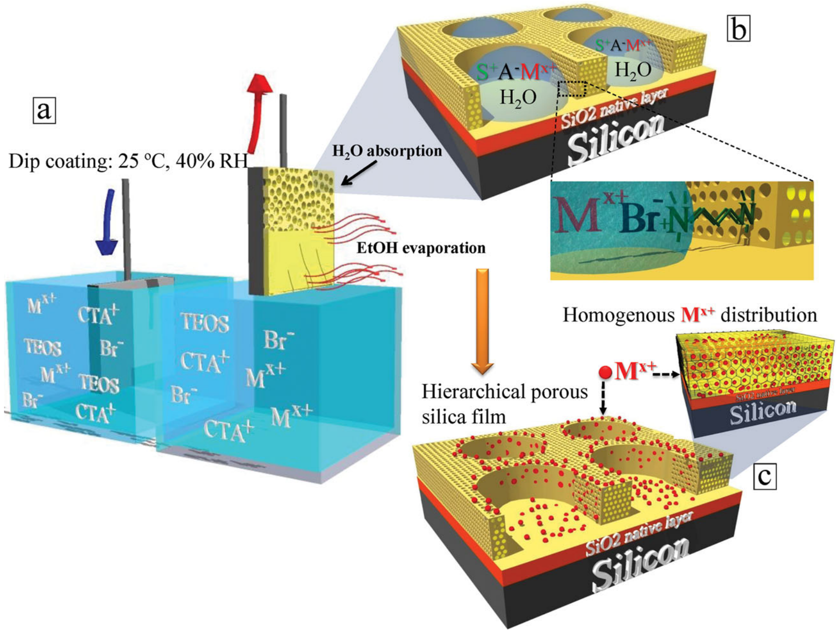

Figure 3. The phase separation mechanism when Br- is used as the counterion: (a) dip-coating deposition of a wet thin film, solvent evaporation and onset of silica condensation; (b) intake of water in the later stages of drying where a hierarchical porosity is produced during a salt-surfactant mediated nucleation and growth mechanism, where droplets are stabilized by a bilayer of CTAB; c) dry film where M^{x+} (Li^+, Na^+, Sr^{2+}, Mn^{2+}, Fe^{2+}/Fe^{3+}, Ca^{2+}, La^{3+}, Ce^{3+}) has been deposited on the walls of the perforations.

2.4. Crystallization of the Silica Films

Among the different cations screened in this work (i.e. Li^+, Na^+, Sr^{2+}, Mn^{2+}, Fe^{2+}/Fe^{3+}, Ca^{2+}, Ce^{3+} and La^{3+}), only Sr^{2+} and Ca^{2+} offer the potential to thermally induce the epitaxial growth of macroperforated (100) α-quartz films on (100) silicon substrates under the conditions studied (see **Table 1**). Significantly, we observe that whereas the Ca^{2+} catalyst acts as a melting agent in a wide range of concentrations, in the case of strontium doped silica films, the crystallization process only takes place under a precise Sr^{2+} salt concentration within the initial precursor solution (see Table 1). **Figure 4** shows a detailed study of crystallization of macroporous silica films at 1000 °C for different Sr^{2+} contents. Noteworthy, only samples with a concentration of 1 mmol of Sr^{2+} (Sr/Si molar ratio of 0.06) within the amorphous silica matrix have the right quantity and homogeneous dispersion of salt to permit further crystallization into a (100) epitaxial quartz film (Figure 4d and e). At this Sr^{2+} concentration, the density, distribution and average diameter of macroperforations within the silica film provides the conditions needed to ensure ultimate epitaxial crystallization. Below this critical concentration (<1 mmol Sr^{2+}), related to an insufficient homogeneity of Sr^{2+} cations within the silica network, film devitrification is impaired and thus so is the

Table 1. Preparation of salt solutions and potential to crystallize prepared films.

Salt	Molarity [mol L^{-1}]	Quantity used [g]	Approximate solution density [g mL^{-1}]	Phase of heat-treated films, 1000 °C
$Ca(NO_3)_2 \cdot 4\,H_2O$	1.00	5.88	1.12	(100)-α-Quartz
$Ca(NO_3)_2 \cdot 4\,H_2O$	3.00	17.74	1.33	(100)-α-Quartz
$CeCl_3 \cdot 7\,H_2O$	1.00	9.38	1.22	Amorphous SiO_2
$CeCl_3 \cdot 7\,H_2O$	2.66	24.78	1.55	Amorphous SiO_2
$FeCl_2 \cdot 4\,H_2O$	1.02	5.05	1.18	Amorphous SiO_2
$La(NO_3)_3 \cdot 6\,H_2O$	1.00	10.83	1.23	Amorphous SiO_2
LiBr	1.00	2.18	1.05	Amorphous SiO_2
$MnCl_2$	1.02	3.20	1.14	Amorphous SiO_2
NaBr	3.01	7.75	1.22	Amorphous SiO_2
$SrCl_2 \cdot 6\,H_2O$	1.01	6.70	1.14	(100)-α-Quartz
$Sr(NO_3)_2$	0.25	1.34	1.03	Amorphous SiO_2
$Sr(NO_3)_2$	0.50	2.65	1.08	Non-oriented α-Quartz
$Sr(NO_3)_2$	1.01	5.32	1.15	(100)-α-Quartz
$Sr(NO_3)_2$	2.00	10.58	1.31	Amorphous SiO_2

subsequent nucleation of quartz crystallites along the silica/silicon interface (see Figure 4f–i). As an example, when 0.5 mmol Sr^{2+} was used (Sr/Si molar ratio of 0.03), a polycrystalline quartz diffraction pattern is observed (Figure 4a), indicating an inhomogeneous and random nucleation of quartz crystals at the interface. Below 0.5 mmol, crystallization was not observed. Conversely, at a Sr/Si molar ratio of 0.12, an excess of catalyst prevents both controlled devitrification and controlled kinetics of nucleation and growth at the interface of SiO_2/Si. Under the right crystallization conditions (i.e. Sr/Si molar ratio of 0.06) a strontium-rich phase sinters during the devitrification and crystallization process to be finally expulsed from the crystalline quartz matrix in the form of spherical nanoparticles. This process will be further developed in the following sections.

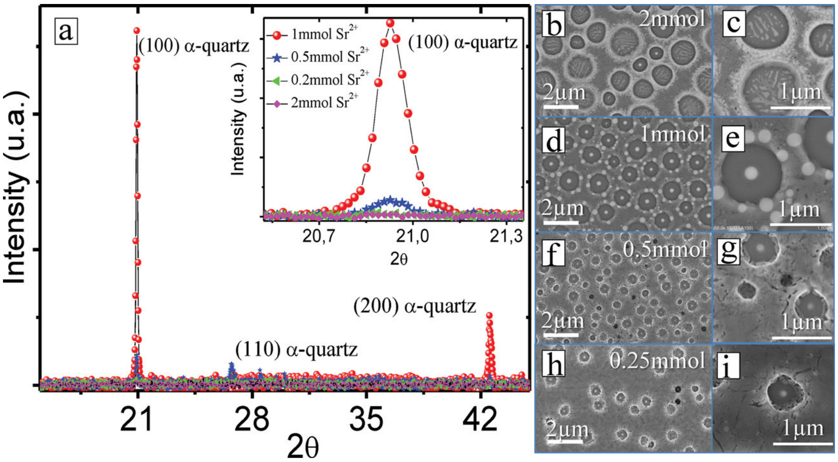

Figure 4. Thermal treatment at 1000 °C of macroporous silica films prepared using different contents of Sr^{2+} relative to 16.3 mmol Si. (a) XRD pattern of samples with 0.25 (green), 0.5 (blue), 1 (red), and 2 (pink) mmol of Sr^{2+}. FEG-SEM images of (b, c) 2 mmol of Sr^{2+}, (d, e) 1 mmol of Sr^{2+}, (f, g) 0.5 mmol of Sr^{2+}, (h, g) 0.25 mmol of Sr^{2+} relative to 16.3 mmol Si.

2.5. Strontium Solid Dewetting Process

In the case of Sr^{2+} doped silica films heated to 900–1000 °C (Figure 4d,e and Figure S6), we observed that strontium dewets or agglomerates at the surface of the quartz film to finally form SrO nanoparticles (**Figure 5**). SrO then reacted with CO_2 and H_2O from the ambient air after cooling to form $SrCO_3$ (Figure S13). This type of behavior has been reported for $La_{0.3}Sr_{0.7}CoO_x$ (LSCO) perovskite membranes during oxygen permeation experiments.[19] In this case, a 10–15 nm surface SrO layer was formed by reduction of the $La_{0.3}Sr_{0.7}CoO_x$ phase at 900 °C. After cooling and exposure to the atmosphere, CO_2 reacted with SrO to form $SrCO_3$, which was identified by XPS.

Evidence for this is also supported by the XPS Sr 3d spectral region. For quartz films, a Sr 3d doublet (Figure S13) showed a shift to higher binding energy, consistent with that expected for a carbonate oxygen.[20] Furthermore, elemental maps of the Sr M-edge around 135 eV and O K-edge around 530 eV, acquired from annular dark field (ADF) Z-contrast image of a macroporous α-quartz layer, allowed us to identify the presence of strontium and oxygen in the carbonaceous amorphous nanoparticles (Figure S13). These observations indicate that the macroporous quartz film has undergone substantial SrO dewetting during the crystallization process to form carbonate species due to the ambient atmosphere. This dewetting process is likely driven by surface energy minimization and occurs via surface diffusion below 800 °C, at which temperature the mobility of the Sr^{2+} atoms is sufficiently high.[21] Figure 5 and Figure S6 show the physical state at different stages of silica crystallization and Sr^{2+} dewetting. This process

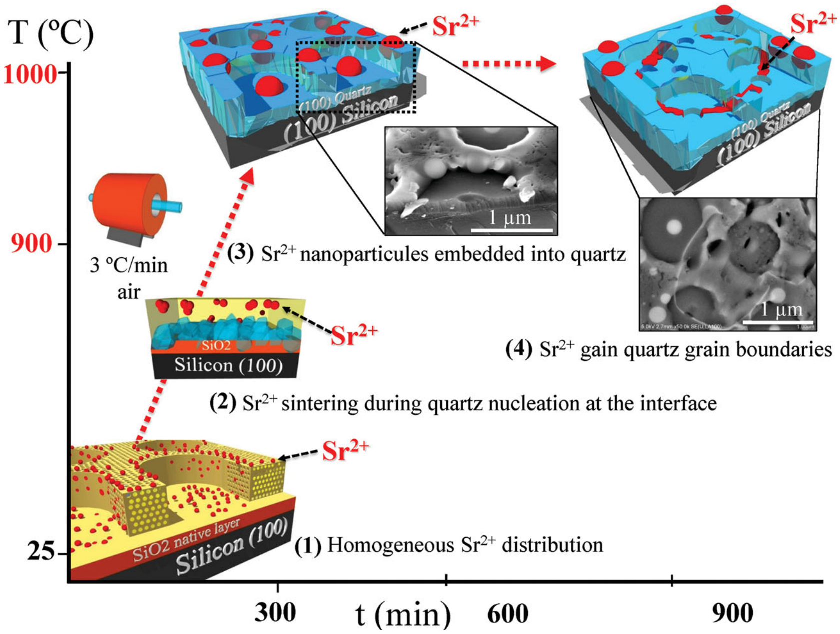

Figure 5. Scheme at different stages of quartz crystallization and Sr^{2+} dewetting. 1) Cross-section of the original mesoporous film showing homogeneous Sr^{2+} distribution within the meso- and macroporous range porous amorphous silica matrix. 2) Nucleation above 800 °C of α-quartz crystals at the silicon-silica interface during the devitrification of the original amorphous mesoporous film. At this stage Sr^{2+} sinters and forms spherical nanoparticles of $SrCO_3$. 3) Oriented columnar quartz crystallite growth within the original (100) silicon substrate, where crystallization is limited by the oxygen diffusion. The catalytic agent (Sr^{2+}, red spheres) used for the devitrification of silica films is trapped within quartz matrix in the form of spherical nanoparticles. 4) Formation mechanism of macrodomains at high temperature (1000 °C) where $SrCO_3$ nanoparticles migrate to the crystal boundaries of the macrodomains.

drives the assembly of sintered $SrCO_3$ nanoparticles at 1000 °C around and at the center of macroperforations (see Figure S6 and Figure S14), which could be useful for electronic and photonic devices and for catalyzing the growth of nanotubes and nanowires.[22,23] In previous studies, we already observed the formation of euhedral macrodomains that break the continuity of quartz films and relax internal stresses within the film at high temperatures.[5] This break results from the difference of thermal expansion coefficients and the relatively high mismatch between the quartz film and the silicon substrate along the α-quartz [010] crystallographic direction at high temperatures (see **Figure 6**a–c). The present work investigates the evolution of the amorphous $SrCO_3$ nanoparticles as they sinter and dewet during thermal treatment. Our results show that sintered amorphous $SrCO_3$ nanoparticles, formed during devitrification and the crystallization process, are expulsed from the interior of the silica matrix towards the quartz macrodomain grain boundaries (Figure 5, step 4). $SrCO_3$ loses its spherical morphology upon insertion into the quartz grain boundaries to minimize the surface energy of the whole system. As a result, new perforations in the quartz film, within the range of 50 nm, are generated from the space previously occupied by those nanoparticles (Figure 5, step 4).

Proof of $SrCO_3$ migration during macrodomain formation is displayed in Figure 6f and Figure S-6, where AFM and FEG-SEM images show the existence of stable $SrCO_3$ particles (brighter spots) along the film. Conversely, within euhedral macrodomains, $SrCO_3$ has migrated to the domain boundaries, leaving behind the particle fingerprint (see AFM profile analysis in Figure 6d).

The converse piezoelectric effect of the macroporous quartz films has been studied by piezo-response force microscopy (PFM). **Figure 7**a shows the topographic AFM image of a crystallized macropore and the corresponding PFM amplitude is displayed in Figure 7b. The PFM response preserves the features of the topographic image, namely the boundaries between the crystals surrounding the macropore and the perimeter of the macropores, but interestingly there are no significant differences between PFM response within and outside the macropore. Thus the piezoelectric functionality of the material is completely preserved.

3. Conclusion

The sol-gel wet deposition approach provides direct access to the integration of piezoelectric macroporous quartz, epitaxially grown on (100)-silicon substrates.

This synthesis method uses a phase separation mechanism and surfactant templating to generate silica films with hierarchical porosity consisting of 3.2 nm mesopores and macropores of between 75 nm – 2 µm. The formation of macroperforations is mediated by the metal salt, counterion, cationic surfactant, the drying time and relative humidity. The hygroscopic phase separation presented here is general for inorganic salts of different nature, being produced using monovalent, divalent and trivalent cations. The phase separation occurred through a nucleation and growth process, controlled both by processing parameters and the chemical composition of the film. In spite of the good control over the final macroperforations, a detailed investigation of the formation mechanism requires further in situ analysis to gather specific kinetics data.

The surfactant plays two roles in the film: it generates mesoporosity and it stabilizes water droplets by minimizing the interfacial energy. GI-SAXS studies may suggest that CTAB micelle organization starts at the silica interface and then propagates further into the film, a subject to be further investigated.

The thermally activated crystallization of the macroporous silica film and the native silica surface is induced by heterogeneous catalysis of Sr^{2+} or Ca^{2+} cations present in the initial precursor solution. A precise concentration and a homogeneous distribution of cations within the silica phase are required. Thus, the interplay between temperature, humidity, catalyst content, and epitaxial growth plays a key role for the bottom-up fabrication of macroporus quartz on silicon substrates. The macroporous structuring of quartz films is in no way detrimental to the piezoelectric properties of the film,

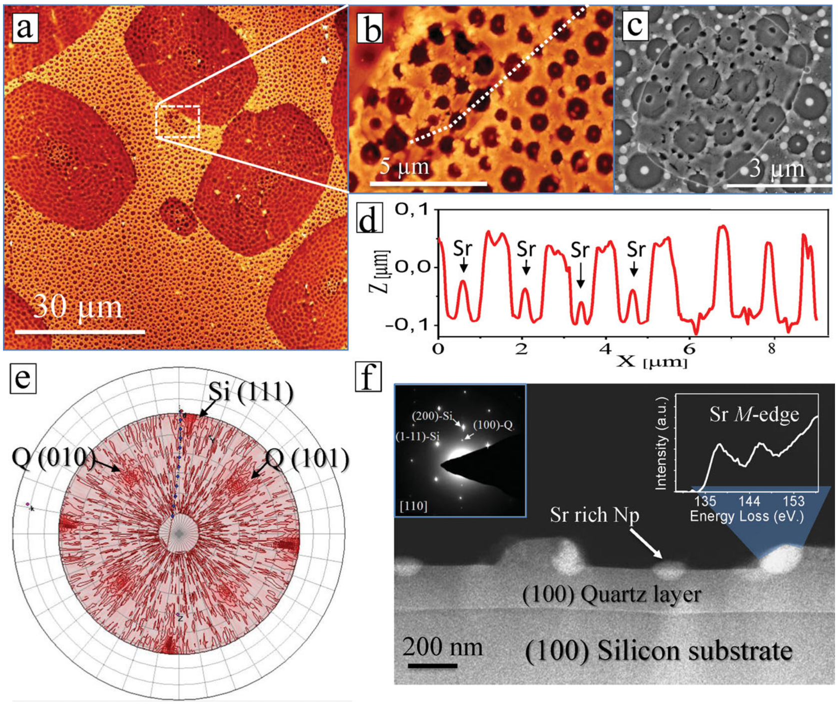

Figure 6. (a) AFM image showing a large scan area of macroporous quartz films prepared at 1000 °C for 5 h. (b,c) Higher magnification AFM and FEG-SEM images illustrating the formation of a thinner euhedral macrodomain (1000 °C over 5 h). (d) Profile analysis of the AFM image in b, revealing that the $SrCO_3$ leaves behind a particle fingerprint upon migration to the grain boundary. (e) Pole figure of macroporous quartz films showing that [210]Q//[100]S is the direction of macroporous quartz growth. (f) Low magnification high angle annular dark field (HAADF) Z-contrast image of a macroporous quartz film grown on the Si substrate assisted by the Sr^{2+} catalyst at 1000 °C, 5 hours. The contrast in the HAADF images is proportional to Z^2 in a first approximation (Z being the atomic number) so that heavier Sr-rich nanoparticles at the surface appear much brighter. Inset figures show the corresponding FFT of both the quartz film and the silicon substrate, and the Sr M-edge EEL spectrum acquired from a Sr-rich nanoparticle.

which are preserved both within the pores and the walls, thus the combination of these two functional properties in the material can be exploited for new developments in biological sensors.

Finally, this work will serve as a starting point for forthcoming studies involving the validation and generalization of sol-gel assisted by a novel phase separation mechanism for the generation of epitaxial quartz macrostructured systems and, more importantly, to improve technological developments based on the fabrication of new high frequency resonators and high sensitivity sensors relevant in different fields of application, opening a wide range of applications.

4. Experimental Section

Materials: Ethanol and 37% HCl, 48% HBr, and 69% HNO_3 were purchased from AnalaR NORMAPUR. Tetraethyl orthosilicate (TEOS), cetyltrimethylammonium bromide (CTAB), manganese chloride, strontium nitrate and strontium chloride hexahydrate were obtained from Aldrich. Calcium nitrate, cerium chloride, ferrous chloride tetrahydrate, lanthanum nitrate and lithium bromide originated from Fluka. CZ silicon wafers doped with boron with a <100> orientation were from SHE Europe Ltd. Water was purified using a MilliQ filter.

To prepare salt solutions of specified molarity, the appropriate amount of salt was weighed into a 25 mL volumetric flask (see Table 1). The salt was then dissolved in purified water, up to the 25 mL mark at 20 °C.

Film Synthesis: In a standard synthesis, CTAB (0.84 g, 2.3 mmol) was dissolved in ethanol (18.9 g, 410 mmol) and 37% HCl (1.6 g, 16.24 mmol H^+, 55.94 mmol H_2O). TEOS (3.4 g, 16.32 mmol) was added dropwise and the solution was aged overnight. A 1 M $SrCl_2$ solution (1.14 g, 1 mmol Sr^{2+}, 52.07 mmol H_2O) was added just before dipping films, yielding a molar ratio of 1 Si: 0.14 CTAB: 6.6 H_2O: 25 EtOH: 1 HCl: 0.06 $SrCl_2$. The solution was not kept for more than a few hours. Any deviation from this standard synthesis is explicitly noted in the text, otherwise it should be assumed that films were prepared using a solution of this composition.

For one set of experiments, either HNO_3 or HBr were substituted for HCl. In this case, the molar ratio of reagents was 1 Si: 0.14 CTAB: 6.6 H_2O: 25 EtOH: 1 HBr or 1 HNO_3: 0.06 $SrCl_2$.

Silicon substrates were rinsed with acetone and water, then soaked in 3M HNO_3 to oxidize the surface of the wafers, then re-rinsed with water, ethanol and wiped with an acetone-soaked tissue prior to use. The films were dip-coated with the solution at 4 mm s^{-1}, 24 °C and 40% RH. The films were then calcined for 5–10 min at 500 °C to remove surfactant. To crystallize, the films were heated at a rate of 3 °C min^{-1} to 900 °C, kept at the maximum temperature for 5 h, and then cooled to room temperature at a rate of 3 °C min^{-1}. Any modifications to this procedure are clearly noted in the text.

X-ray Diffraction (XRD): The crystalline texture of films was studied with a Bruker D8 diffractometer: 3 s acquisition every 0.02° in Bragg-Brentano geometry. Epitaxial relationship was analyzed through X-ray diffraction measurements by using a Bruker AXS GADDS equipped with a 2D X-ray detector. Diffraction patterns were measured with X-ray radiation of wavelength 0.154056 nm.

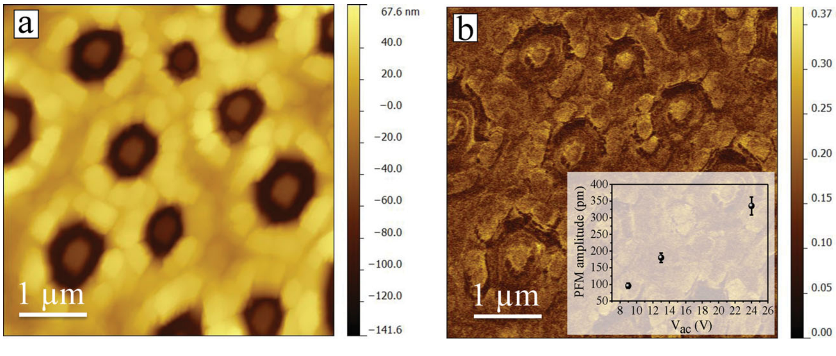

Figure 7. Piezoelectric response of macroperforated epitaxial quartz films. (a) AFM image of the topography and (b) PFM amplitude recorded simultaneously under a tip-substrate AC voltage of 17.5 V. The inset shows the proportional relationship between applied voltage and tip deflection.

Grazing Incidence Small Angle X-ray Scattering (GI-SAXS): A Rigaku S-max 3000 equipped with a microfocus source l ¼ 0.154 nm and a 2D Gabriel type detector was placed at 1480 mm from the sample (all under vacuum), at an incident angle of 0.2°. The direct and specular reflected beams were masked by a vertical beam-stop. Diffraction patterns were analyzed using Igor software 13.

Field Emission Gun Scanning Electron Microscope (FEG-SEM): The microstructure of the films was studied using FEG-SEM model Su-70 Hitachi, equipped with an EDX detector X-max 50 mm^2 Oxford instruments.

Transmission Electron Microscope (TEM): The microstructure of the films was studied using a FEI Technai G2 F20 operated at 200 kV, in both TEM and STEM mode, and equipped with a Gatan Imaging Filter (GIF) Quantum SE 963 spectrometer. Specimens for TEM were prepared by conventional methods, by grinding, dimpling and Ar ion milling.

X-ray Photoelectron Spectroscopy (XPS): XPS measurements were carried out in a Vacuum Science Workshop (VSW) chamber (base pressure $< 10^{-9}$), equipped with a monochromatic X-ray source AlKα (1486.6 eV). The angle between the X-ray source and the photoelectron detector is set at the “magic angle”, i.e. 54.7°. All the spectra were recorded in the direction normal to the sample surface.

Atomic Force Microscopy (AFM): AFM imaging experiments were performed on a multimode-V microscope controlled by Nanoscope-V electronics and the Nanoscope 8 software (Bruker AXS Corporation, Santa Barbara, CA). V-shaped Si_3N_4 cantilevers (SNL, Bruker AXS Corporation, Santa Barbara, CA), with a nominal spring constant of 0.35 N/m, a nominal resonant frequency of 65 kHz and a nominal tip radius of 3 nm, were operated under air.

Piezoresponse Force Microscopy (PFM): Piezoresponse force microscopy measurements were performed on an Agilent 5500LS instrument using a conducting tip of Si coated with boron-doped diamond with a spring constant of 0.2 N/m. The tip was brought into feedback position in the contact mode with a constant force of 25 nN which was maintained between the tip and the sample surface. An AC voltage $V_{AC} = 7.5$ V was applied between the tip and the substrate backside and a frequency sweep was recorded to determine the frequency of the contact resonance peak (145 kHz) and its quality factor (Q = 49). The tip oscillation amplitude driven by the oscillating surface displacement of the film was recorded with a lock-in amplifier while applying between the tip and the substrate backside a V_{AC} of 17.5 V at 145 kHz. The photodetector response was calibrated with a force-displacement curve to obtain the response in units of distance. The tip amplitudes presented in Figure 7(b) was corrected by subtracting the zero volt amplitude and dividing by Q.

Supporting Information

Supporting Information is available from the Wiley Online Library or from the author.

Acknowledgements

G. L. Drisko and A. Carretero-Genevrier contributed equally to this work. ACG and GLD acknowledge the Collège de France foundation for material and a part of their financial support and IMPC for use FEG-SEM facilities. ACG acknowledges Collège de France and LCMCP for his Visiting Scientist position and INL-CNRS for his detachment. This study was made possible by grant, Marie Curie Reintegration Grant (PCIG09-GA-2011–294168) to M.G. We thank David Montero and Mohamed Selmane for technical support. Andrés Gomez is acknowledged for his technical assistance in the PFM measurements. Geneviève Grenet is acknowledged for her technical assistance in XPS measurements at INL-CNRS. This research was partially funded by the RyC-2012–11709 contract of J. G. The TEM microscopy work was conducted in the Catalan Institute of Nanoscience and Nanotechnology (ICN2). Authors acknowledge the ICN2 Electron Microscopy Division for offering access to their instruments and expertise.

Received: April 3, 2014
Revised: May 10, 2014

[1] L. Li, C. Chen, J. Li, A. Zhang, X. Liu, B. Xu, S. Gao, G. Jin, Z. Ma, *J. Mater. Chem.* **2009**, *19*, 2789.
[2] C. J. Brinker, P. G. Clem, *Science* **2013**, *340*, 818.
[3] S. Tadigadapa, K. Mateti, *Meas. Sci. Technol.* **2009**, *20*, 092001.
[4] K. Mohamed, M. M. Alkaisi, *Nanotechnology* **2013**, *24*, 015302.
[5] A. Carretero-Genevrier, M. Gich, L. Picas, J. Gazquez, G. L. Drisko, C. Boissiere, D. Grosso, J. Rodriguez-Carvajal, C. Sanchez, *Science* **2013**, *340*, 827.
[6] L. Malfatti, P. Falcaro, D. Marongiu, M. F. Casula, H. Amenitsch, P. Innocenzi, *Chem. Mater.* **2009**, *21*, 4846.
[7] L. Malfatti, M. G. Bellino, P. Innocenzi, G. J. A. A. Soler-Illia, *Chem. Mater.* **2009**, *21*, 2763.
[8] L. Han, P. Xiong, J. Bai, S. Che, *J. Am. Chem. Soc.* **2011**, *133*, 6106.
[9] L. Heng, B. Wang, M. Li, Y. Zhang, L. Jiang, *Materials* **2013**, *6*, 460.
[10] M. Faustini, B. Louis, P. A. Albouy, M. Kuemmel, D. Grosso, *J. Phys. Chem. C* **2010**, *114*, 7637.
[11] X. Jiang, T. L. Ward, F. van Swol, C. Brinker, *J. Ind. Eng. Chem. Res.* **2010**, *49*, 5631.
[12] *CRC Handbook of Chemistry and Physics*, 85th Ed (Ed: D. R. Lide), CRC Press, Boca Raton, FL **2005**.
[13] T. A. Bleasdale, G. J. T. Tiddy, E. Wyn-Jones, *J. Phys. Chem. C* **1991**, *95*, 5385.
[14] C. Boissiere, D. Grosso, A. Chaumonnot, L. Nicole, C. Sanchez, *Adv. Mater.* **2011**, *23*, 599.
[15] Q. Huo, D. I. Margolese, U. Ciesla, D. G. Demuth, P. Feng, T. E. Gier, P. Sieger, A. Firouzi, B. F. Chemelka, F. Schüth, G. D. Stucky, *Chem. Mater.* **1994**, *6*, 1176.
[16] S. H. Wu, D. H. Chen, *J. Colloid Interface Sci.* **2004**, *273*, 165.
[17] Z. M. Sui, X. Chen, L. Y. Wang, L. M. Xu, W. C. Zhuang, Y. C. Chai, C. Yang, *J. Phys. E-Low Dimensional Systems Nanostructures* **2006**, *33*, 308.
[18] J. Casas, M. Venkataramasubramani, Y. Wang, L. Tang, *Biosens. Bioelectron.* **2013**, *49*, 525.
[19] R. H. E. van Doorn, H. J. M. Bouwmeester, A. Burggraaf, *J. Solid-State Ionics* **1998**, *111*, 263.
[20] J. F. Moulder, W. F. Stickle, P. E. Sobol, K. D. Bomben, *Perkin Elmer Corporation*, Physical Electronics Division, Eden Prairie, Minnesota **1992**.
[21] C. V. Thompson, *Annu. Rev. Mater. Res.* **2012**, *42*, 399.
[22] A. Carretero-Genevrier, T. Puig, X. Obradors, N. Mestres, *Chem. Soc. Rev.* **2014**, *43*, 2042.
[23] A. Carretero-Genevrier, J. Oro-Sole, J. Gazquez, C. Magén, L. Miranda, T. Puig, X. Obradors, E. Ferain, C. Sanchez, J. Rodriguez-Carvajal, N. Mestres, *Chem. Mater.* **2014**, *26*, 1019.